RESEARCH PAPER

A locally conservative finite element framework for the simulation of coupled flow and reservoir geomechanics

Birendra Jha · Ruben Juanes

Abstract In this paper, we present a computational framework for the simulation of coupled flow and reservoir geomechanics. The physical model is restricted to Biot's theory of single-phase flow and linear poroelasticity, but is sufficiently general to be extended to multiphase flow problems and inelastic behavior. The distinctive technical aspects of our approach are: (1) the space discretization of the equations. The unknown variables are the pressure, the fluid velocity, and the rock displacements. We recognize that these variables are of very different nature, and need to be discretized differently. We propose a mixed finite element space discretization, which is stable, convergent, locally mass conservative, and employs a single computational grid. To ensure stability and robustness, we perform an implicit time integration of the fluid flow equations. (2) The strategies for the solution of the coupled system. We compare different solution strategies, including the fully coupled approach, the usual (conditionally stable) iteratively coupled approach, and a less common unconditionally stable sequential scheme. We show that the latter scheme corresponds to a modified block Jacobi method, which also enjoys improved convergence properties. This computational model has been implemented in an object-oriented reservoir simulator, whose modular design allows for further extensions and enhancements. We show several representative numerical simulations that illustrate the effectiveness of the approach.

Keywords Geomechanics · Iteratively coupled · Local mass conservation · Mixed finite elements · Oil and gas · Poroelasticity · Reservoir · Unconditionally stable · Undrained split

1 Introduction

Reservoir geomechanics is concerned with the simultaneous study of fluid flow and the mechanical response of the reservoir. Quantification of the state of deformation and stress of the reservoir is essential for the correct prediction of a number of processes of enormous economic impact, such as primary compaction drive, waterflooding, surface subsidence, seal integrity, hydrofracturing, sand production and well failure.

The strong interaction between multiphase flow and deformation of the reservoir is evidenced by a number of notable case histories. For example, the Wilmington field, located in Long Beach (California), experienced a maximum subsidence of about 9 m as a result of oil production for over 20 years. Associated with surface subsidence, maximum horizontal displacements as large as 3.7 m were recorded [2]. Another well-known case is the Ekofisk field, in the Norwegian sector of the North Sea. A subsidence bowl was discovered in 1984 and, by 1989, subsidence had reached a maximum value of over 4 m. The cost of raising platforms and protecting storage facilities exceeded $400 million [17]. Another dramatic consequence of the coupling between fluid flow and rock deformation is well

B. Jha
Occidental Oil and Gas Corporation,
111 W Ocean Blvd., 7th Floor,
Long Beach, CA 90802, USA
e-mail: birendra_jha2@oxy.com

R. Juanes (✉)
Department of Civil and Environmental Engineering,
Massachusetts Institute of Technology,
77 Massachusetts Ave., Room 48-319,
Cambridge, MA 02139, USA
e-mail: juanes@mit.edu

failure. The severity of wellbore instability can be over-whelming: at the Belridge diatomite field, located 45 miles west of Bakersfield (California), nearly 1,000 wells have experienced serious casing damage during the past 20 years of production [14]. Another illustrative case history is that of the Matagorda Island 623 field in the Gulf of Mexico, where all 17 wells have experienced some form of well failure [23]. Overall, it is estimated that the cost associated with wellbore instability is at least one billion dollars per year worldwide [1].

Theoretical and practical difficulties have prevented coupled geomechanical models from being used routinely in oil and gas reservoir simulation studies. Some of these challenges are the complex mechanical behavior of ge-omaterials, the strong coupling between the mechanical and fluid flow problems, and the fact that the reservoir models become very computationally intensive.

Over the past decade, however, reservoir geomechanics has emerged as a necessary integral part of reservoir simulation studies [30, 31], recognizing that the usual treatment of mechanical deformation by means of the rock compressibility is far from adequate. Simulation models include: (1) finite difference and finite volume procedures, limited to elastic response or explicit treatment of plasticity [27, 32, 34, 35]; (2) finite element procedures for the mechanics without coupling with the flow field [16, 25]; (3) finite elements for the mechanics problem and finite volumes for the flow problem, limited to poroelastic behavior [13, 15]; and (4) fully coupled, finite element models for flow and mechanics [11, 21, 22, 24, 39, 40]. All of these models are based on the displacement formulation of the linear momentum balance equation.

A topic that has drawn significant attention is that of coupling strategies for the solution of the flow and mechanics problems [13]. They range from one-way coupling [14] to loose or explicit coupling [26], iterative coupling [18, 31, 37, 38, 42] and fully coupled approaches [11, 21].

In this paper we develop a computational model for the simulation of coupled flow and geomechanics [19]. The physical model is restricted to Biot's theory of single-phase flow and linear poroelasticity [7], but is sufficiently general to be extended to multiphase flow problems and inelastic behavior. The proposed scheme employs a finite element method for the mechanical problem and a mixed finite element method for the flow problem. This scheme gives rise to a natural and elegant discretization of the equations. The practical benefit of this formulation is that only one simulation grid needs to be defined. Moreover, the grid can be unstructured and consist of both hexahedra and tetra-hedra. The proposed spatial discretization leads to a scheme that is locally mass conservative and provides an accurate calculation of fluid velocities.

The numerical model described above leads to a system of nonlinear algebraic equations that needs to be solved at every time step. The solution of the coupled flow-deformation system can be attempted using explicitly coupled, iteratively coupled, or fully coupled approaches. We investigate the use of an unconditionally stable, iteratively coupled method [3, 4, 28, 42], whose obvious benefit is that the time step size is only limited by accuracy considerations, and not stability. We compare the performance of this unconditionally stable scheme with a fully coupled approach and the standard sequential scheme (which is only conditionally stable).

An outline of the paper is as follows. In Sect. 2, we describe the physical and mathematical model of single-phase flow and geomechanics. In Sect. 3 we formulate the mixed finite element discretization of the governing equations that leads to the fully discrete coupled system. We then describe, in Sect. 4, different solution procedures for the coupled system, with special attention to staggered (or sequential) solution schemes. We apply the proposed formulation to a number of representative numerical simulations in Sect. 5. Finally, in Sect. 6, we gather the main conclusions of this investigation.

2 Physical and mathematical model

As in all macroscopic models of porous media, we adopt a continuum representation, in which fluid and solid are viewed as overlapping continua [12]. We restrict the physical model to Biot's self-consistent theory of poro-elasticity [7, 12, 41]. In particular, our model is limited by the following assumptions: (1) single-phase flow; (2) slightly compressible fluid; (3) small deformations; (4) linear elastic and isotropic material behavior; (5) no stress dependence of flow properties like porosity and perme-ability; (6) isothermal system. In what follows we pose the balance laws and constitutive relations. We also express the governing equations in weak form, which will provide the starting point for the mixed finite element discretization.

2.1 Balance laws

The equations governing the coupled pore fluid–solid system in a porous medium are balance laws expressing conservation of fluid mass and balance of linear momentum.

2.1.1 Balance of fluid mass

Let Ω be the domain of interest, the governing equation for fluid mass reads:

$$\frac{\partial m}{\partial t} + \nabla \cdot \boldsymbol{F} = \rho_{\mathrm{fl}} f \quad \text{in } \Omega. \tag{1}$$

In the equation above m is the fluid mass content (fluid mass per unit volume of porous medium), $\boldsymbol{F} = \rho_{\mathrm{fl}} \boldsymbol{v}$ is the mass flux (fluid mass flow rate per unit area and time), ρ_{fl} is the fluid density, $\boldsymbol{v}$ is the Darcy velocity, and f is a source term.

It will be useful to define the fluid content variation ζ:

$$\zeta := \frac{\delta m}{\rho_{\mathrm{fl},0}}, \tag{2}$$

where $\delta m = m - m_0$ is the increment in fluid mass content with respect to the initial reference state, and $\rho_{\mathrm{fl},0}$ is the reference fluid density.

2.1.2 Balance of linear momentum

In the quasi-static limit of interest, the local equation of mechanical equilibrium of the solid–fluid system reads:

$$\nabla \cdot \boldsymbol{\sigma} + \rho \boldsymbol{g} = \boldsymbol{0}, \tag{3}$$

where $\boldsymbol{\sigma}$ is the total (Cauchy) stress tensor, $\boldsymbol{g}$ is the gravitational acceleration, and ρ is the bulk density defined in terms of the mixture constituents by:

$$\rho = \phi \rho_{\mathrm{fl}} + (1 - \phi) \rho_{\mathrm{s}}, \tag{4}$$

where ρ_{s} is the density of the solid phase and ϕ is the porosity.

2.2 Constitutive relations

The poromechanical behavior of the system considered in this paper is described by Darcy's law and the Biot equations of poroelasticity.

2.2.1 Darcy's law

The Darcy velocity $\boldsymbol{v}$ is linked to the fluid pressure p by:

$$\boldsymbol{v} = -\frac{\mathbf{k}}{\mu} (\nabla p - \rho_{\mathrm{fl}} \boldsymbol{g}), \tag{5}$$

where $\mathbf{k}$ is the absolute permeability and μ is the fluid viscosity.

2.2.2 Biot's equations of poroelasticity

The self-consistent theory of poroelastic behavior proposed by Biot [7] links the changes in total stress and fluid pressure with changes in strain and fluid content. We write these expressions in the following (mixed stiffness) incremental form [41]:

$$\delta\boldsymbol{\sigma} = \boldsymbol{C} : \boldsymbol{\varepsilon} - b\delta p \mathbf{1}, \tag{6}$$

$$\zeta = b\varepsilon_V + M^{-1}\delta p. \tag{7}$$

In the equations above, $\boldsymbol{C}$ is the (drained) rank-4 elasticity tensor, and b and M are the Biot coefficient and the Biot modulus, respectively. $\boldsymbol{\varepsilon}$ is the linearized strain tensor, defined as the symmetric gradient of the displacement $\boldsymbol{u}$:

$$\boldsymbol{\varepsilon} = \nabla^s \boldsymbol{u} = \frac{1}{2} (\nabla \boldsymbol{u} + \nabla^t \boldsymbol{u}). \tag{8}$$

The (rank-2) strain tensor can be expressed as a sum of its volumetric and deviatoric parts:

$$\boldsymbol{\varepsilon} = \frac{1}{3} \varepsilon_V \mathbf{1} + \boldsymbol{e}, \tag{9}$$

where $\varepsilon_V = \mathrm{trace}\,\boldsymbol{\varepsilon}$ is the volumetric strain, $\mathbf{1}$ is the rank-2 identity tensor, and $\boldsymbol{e}$ is the deviatoric part of the strain tensor. A thorough explanation of the physical meaning of the Biot equations and the parameters involved is given elsewhere [12, 41].

We note that, using the volumetric–deviatoric decomposition of the strain tensor, Eq. (6) takes the form:

$$\delta\boldsymbol{\sigma} = (K\varepsilon_V \mathbf{1} + 2G\boldsymbol{e}) - b\delta p \mathbf{1}, \tag{10}$$

where K is the *drained* bulk modulus, and G is the shear modulus. Using Eq. (7), the equation above may be written in the following form:

$$\delta\boldsymbol{\sigma} = (K_u \varepsilon_V \mathbf{1} + 2G\boldsymbol{e}) - bM\zeta \mathbf{1}, \tag{11}$$

where $K_u = K + b^2 M$ is the *undrained* bulk modulus. The terms drained and undrained refer to processes under which $\delta p = 0$ (constant pressure) and $\zeta = 0$ (constant fluid volume), respectively. Such distinction will be essential when defining the sequential solution strategies of the coupled system.

2.3 Boundary and initial conditions

The mathematical model requires that initial and boundary conditions be defined for both the fluid flow and mechanical problems. We consider the following boundary conditions for the flow problem:

$$p = \bar{p} \text{ on } \Gamma_p, \quad \boldsymbol{v} \cdot \boldsymbol{n} = \bar{v} \text{ on } \Gamma_v, \tag{12}$$

where $\bar{p}$ is a prescribed pressure, and $\bar{v}$ is a prescribed volumetric flux, and $\boldsymbol{n}$ is the outward unit normal to the

boundary $\partial\Omega$. The parts of the boundary with prescribed pressure and flux must be non-overlapping and cover the entire boundary, that is,

$$\Gamma_p \cap \Gamma_v = \emptyset, \quad \Gamma_p \cup \Gamma_v = \partial\Omega. \tag{13}$$

Similarly, we consider the following boundary conditions for the equilibrium equations:

$$\boldsymbol{u} = \bar{\boldsymbol{u}} \text{ on } \Gamma_u, \quad \boldsymbol{\sigma} \cdot \boldsymbol{n} = \bar{\boldsymbol{t}} \text{ on } \Gamma_\sigma, \tag{14}$$

where $\bar{\boldsymbol{u}}$ is a prescribed displacement, and $\bar{\boldsymbol{t}}$ is a prescribed traction. Again, Γ_u and Γ_σ must satisfy:

$$\Gamma_u \cap \Gamma_\sigma = \emptyset, \quad \Gamma_u \cup \Gamma_\sigma = \partial\Omega. \tag{15}$$

The poroelasticity problem must be initialized with a pressure field, $p|_{t=0} = p_0$, and initial stresses $\boldsymbol{\sigma}|_{t=0} = \boldsymbol{\sigma}_0$ (the initial displacements are assumed to be zero). We should mention that, in practice, initialization of coupled geomechanical models is a thorny issue. The prescribed initial stresses prior to reservoir recovery have a significant impact on the numerical results [14]. Vertical stresses are often known with reasonable accuracy, based on gravitational loading. On the other hand, horizontal stresses are much more uncertain [43].

2.4 Weak form of the equations

Let us give a summary of the governing equations of the coupled poroelasticity problem described above:

$$(\mathbf{k}/\mu)^{-1}\boldsymbol{v} + \nabla p = \rho_{\text{fl}}\boldsymbol{g} \quad \text{(Darcy's law),} \tag{16}$$

$$\frac{\partial\zeta}{\partial t} + \nabla \cdot \boldsymbol{v} = f \quad \text{(fluid mass balance),} \tag{17}$$

$$\nabla \cdot \boldsymbol{\sigma} = -\rho\boldsymbol{g} \quad \text{(momentum balance).} \tag{18}$$

We have assumed, for simplicity, that the mass flux is evaluated using the reference density $\rho_{\text{fl,0}}$.

The starting point for the finite element model presented in the next section is the weak (variational) form of the problem, which we now discuss. The governing equations (together with the initial and boundary conditions) are solved for the Darcy velocity $\boldsymbol{v}$, pressure p and displacement $\boldsymbol{u}$. The regularity requirements for each of these variables is different. The pressure must belong to the space $L^2(\Omega)$ of square integrable functions in Ω:

$$L^2(\Omega) = \left\{ p : \int_\Omega |p|^2 \, \mathrm{d}\Omega < +\infty \right\}. \tag{19}$$

The displacement must satisfy stricter regularity conditions. Each component of the displacement and its

first derivatives must belong to L^2, and therefore, $\boldsymbol{u} \in (H^1(\Omega))^d$, where d is the number of space dimensions and:

$$H^1(\Omega) = \left\{ u : u \in L^2(\Omega), Du \in L^2(\Omega) \right\}. \tag{20}$$

The velocity must admit well-defined (continuous) normal traces. Physically, the integral of the normal trace of the velocity field along a boundary is precisely the volumetric flux across this boundary. The space with the proper regularity for the velocity is:

$$H(\text{div}, \Omega) = \left\{ \boldsymbol{v} : \boldsymbol{v} \in (L^2(\Omega))^d, \nabla \cdot \boldsymbol{v} \in L^2(\Omega) \right\}. \tag{21}$$

Let us now define the following solution function spaces for the velocity and displacement (satisfying the essential boundary conditions):

$$\mathcal{V} = \{ \boldsymbol{v} : \boldsymbol{v} \in H(\text{div}, \Omega), \boldsymbol{v} \cdot \boldsymbol{n} = \bar{v} \text{ on } \Gamma_v \}, \tag{22}$$

$$\mathcal{U} = \left\{ \boldsymbol{u} : \boldsymbol{u} \in (H^1(\Omega))^d, \boldsymbol{u} = \bar{\boldsymbol{u}} \text{ on } \Gamma_u \right\}, \tag{23}$$

and the corresponding test function spaces (satisfying the homogenous counterpart of the essential boundary conditions):

$$\mathcal{V}_0 = \{ \boldsymbol{v} : \boldsymbol{v} \in H(\text{div}, \Omega), \boldsymbol{v} \cdot \boldsymbol{n} = 0 \text{ on } \Gamma_v \}, \tag{24}$$

$$\mathcal{U}_0 = \left\{ \boldsymbol{u} : \boldsymbol{u} \in (H^1(\Omega))^d, \boldsymbol{u} = \boldsymbol{0} \text{ on } \Gamma_u \right\}. \tag{25}$$

We also define the pressure function space $\mathcal{Q} = L^2(\Omega)$.

Using standard arguments (that is, multiplying by the test functions, integrating over the domain, applying the divergence theorem, inserting the essential and natural boundary conditions, and exploiting symmetry of the stress tensor), we arrive at the weak form of the problem:

At each time $t > 0$, find $(\boldsymbol{v}, p, \boldsymbol{u}) \in \mathcal{V} \times \mathcal{Q} \times \mathcal{U}$ such that:

$$\int_\Omega \boldsymbol{\psi} \cdot (\mathbf{k}/\mu)^{-1}\boldsymbol{v}\,\mathrm{d}\Omega - \int_\Omega \nabla \cdot \boldsymbol{\psi} p\,\mathrm{d}\Omega$$
$$= \int_\Omega \boldsymbol{\psi} \cdot \rho_{\text{fl}}\boldsymbol{g}\,\mathrm{d}\Omega - \int_{\Gamma_p} \boldsymbol{\psi} \cdot \boldsymbol{n}\bar{p}\,\mathrm{d}\Gamma, \tag{26}$$

$$\int_\Omega \varphi \frac{\partial\zeta}{\partial t}\,\mathrm{d}\Omega + \int_\Omega \varphi\nabla \cdot \boldsymbol{v}\,\mathrm{d}\Omega = \int_\Omega \varphi f\,\mathrm{d}\Omega, \tag{27}$$

$$\int_\Omega \nabla^s\boldsymbol{\eta} : \boldsymbol{\sigma}\,\mathrm{d}\Omega = \int_\Omega \boldsymbol{\eta} \cdot \rho\boldsymbol{g}\,\mathrm{d}\Omega + \int_{\Gamma_\sigma} \boldsymbol{\eta} \cdot \bar{\boldsymbol{t}}\,\mathrm{d}\Gamma, \tag{28}$$

for all $\boldsymbol{\psi} \in \mathcal{V}_0, \varphi \in \mathcal{Q}$ and $\boldsymbol{\eta} \in \mathcal{U}_0$. The problem (26–28), together with appropriate initial conditions, admits a unique solution.

3 Numerical model: discretization

In this section we discuss the numerical discretization of the coupled flow and geomechanics problem. We first present the space discretization, followed by the time discretization and, finally, the fully discrete system of algebraic equations.

3.1 Space discretization

The essential observation is that the pressure, velocity and displacements have very different regularity requirements and, therefore, must be discretized differently. This feature sets our numerical model apart from traditional reservoir simulators—where virtually all variables are assumed to be constant over each gridblock—and from most numerical models in geotechnical engineering—which use a nodal-based finite element discretization for all the unknowns. The design conditions (and main benefits) of our space discretization are the following: (1) local mass conservation at the element level; (2) continuous displacement field, which permits to track the actual deformation of the porous medium; (3) stable, convergent approximation with the lowest-order discretization; and (4) single, unstructured computational grid.

The proposed scheme employs a mixed finite element method based on the weak form of the problem (26–28). More specifically, we choose a *conforming* mixed finite element method. Let $\mathcal{T}_h$ be a partition of the domain into nonoverlapping elements or gridblocks E_j, such that $\Omega = \bigcup_{j=1}^{n_{\text{elem}}} E_j$. On this grid, we shall define the spaces $\mathcal{V}_h, \mathcal{Q}_h$ and $\mathcal{U}_h$ as finite-dimensional subspaces of $\mathcal{V}, \mathcal{Q}$ and $\mathcal{U}$, respectively, and the corresponding test function spaces $\mathcal{V}_{h,0}$ and $\mathcal{U}_{h,0}$. The discrete mixed finite element approximation of the continuum problem (26–28) reads:

At each time $t > 0$, find $(\mathbf{v}_h, p_h, \mathbf{u}_h) \in \mathcal{V}_h \times \mathcal{Q}_h \times \mathcal{U}_h$ such that:

$$\int_\Omega \boldsymbol{\psi}_h \cdot (\mathbf{k}/\mu)^{-1} \mathbf{v}_h \mathrm{d}\Omega - \int_\Omega \nabla \cdot \boldsymbol{\psi}_h p_h \mathrm{d}\Omega$$
$$= \int_\Omega \boldsymbol{\psi}_h \cdot \rho_{\text{fl}} \mathbf{g} \mathrm{d}\Omega - \int_{\Gamma_p} \boldsymbol{\psi}_h \cdot \mathbf{n}\bar{p} \mathrm{d}\Gamma, \tag{29}$$

$$\int_\Omega \varphi_h \frac{\partial \zeta_h}{\partial t} \mathrm{d}\Omega + \int_\Omega \varphi_h \nabla \cdot \mathbf{v}_h \mathrm{d}\Omega = \int_\Omega \varphi_h f \mathrm{d}\Omega, \tag{30}$$

$$\int_\Omega \nabla^s \boldsymbol{\eta}_h : \boldsymbol{\sigma}_h \mathrm{d}\Omega = \int_\Omega \boldsymbol{\eta}_h \cdot \rho \mathbf{g} \mathrm{d}\Omega + \int_{\Gamma_\sigma} \boldsymbol{\eta}_h \cdot \bar{\mathbf{t}} \mathrm{d}\Gamma, \tag{31}$$

for all $\boldsymbol{\psi}_h \in \mathcal{V}_{h,0}, \varphi_h \in \mathcal{Q}_h$ and $\boldsymbol{\eta}_h \in \mathcal{U}_{h,0}$.

This finite-dimensional spaces cannot be chosen independently. To obtain a convergent approximation, they must satisfy two conditions [8, 10]: a standard coercivity condition, and the discrete inf-sup condition [6, 9]. In this work, we employ the lowest-order continuous finite element spaces for the displacement, the lowest-order Raviart–Thomas [29] space for the velocity (RT_0), and the space of piecewise constants for the pressure. As a result, the velocity, pressure and displacement fields are interpolated as follows:

$$\mathbf{v}_h = \sum_{l=1}^{n_{\text{face}}} \boldsymbol{\psi}_l V_l, \tag{32}$$

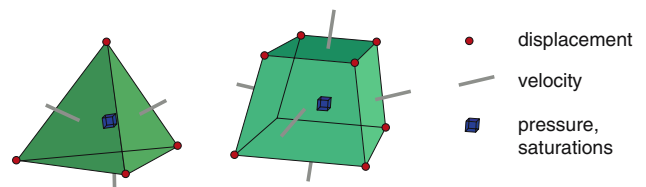$$p_h = \sum_{j=1}^{n_{\text{elem}}} \varphi_j P_j, \tag{33}$$

$$\mathbf{u}_h = \sum_{b=1}^{n_{\text{node}}} \eta_b \mathbf{U}_b, \tag{34}$$

where V_l are the volumetric fluxes through element faces, P_j are the element pressures, and $\mathbf{U}_b$ are the displacements at the element nodes (vertices). The location of the degrees of freedom is shown in Fig. 1 for three-dimensional tetrahedral and hexahedral elements.

The displacement interpolation functions η_b are the usual finite element hat functions, which take a value of 1 at node b, and 0 at all other nodes. The pressure interpolation functions φ_j are discontinuous functions that take a constant value of 1 at element j, and 0 at all other elements. The velocity interpolation functions $\boldsymbol{\psi}_l$ are *vector* functions that satisfy the following condition: they produce a unit flux through face l and 0 through all other faces. In Fig. 2 we plot the RT_0 shape function for one of the edges on triangular and quadrilateral reference elements.

The semi-discrete finite element equations are obtained by inserting the interpolation (32–34) and testing Eqs. (29–31) against each individual shape function. In residual form, the semi-discrete finite element equations read:

$$0 = \int_\Omega \boldsymbol{\psi}_k \cdot \rho_{\text{fl}} \mathbf{g} \mathrm{d}\Omega - \int_{\Gamma_p} \boldsymbol{\psi}_k \cdot \mathbf{n}\bar{p} \mathrm{d}\Gamma$$
$$- \int_\Omega \boldsymbol{\psi}_k \cdot (\mathbf{k}/\mu)^{-1} \mathbf{v}_h \mathrm{d}\Omega + \int_\Omega \nabla \cdot \boldsymbol{\psi}_k p_h \mathrm{d}\Omega, \tag{35}$$

• displacement
— velocity
▪ pressure, saturations

Fig. 1 Location of the different unknowns (displacements, fluid velocity, fluid pressure and fluid saturations) on tetrahedral and hexahedral grid blocks
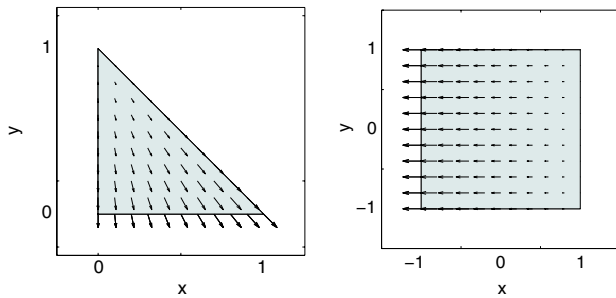
Fig. 2 RT_0 shape function for one of the edges on the triangular and quadrilateral reference elements

$$0 = \int_\Omega \varphi_i f \mathrm{d}\Omega - \int_\Omega \varphi_i \nabla \cdot \boldsymbol{v}_h \mathrm{d}\Omega - \int_\Omega \varphi_i \frac{\partial \zeta_h}{\partial t} \mathrm{d}\Omega, \quad (36)$$

$$0 = \int_\Omega \eta_a \rho \boldsymbol{g} \mathrm{d}\Omega + \int_{\Gamma_\sigma} \eta_a \bar{\boldsymbol{t}} \mathrm{d}\Gamma - \int_\Omega \boldsymbol{B}_a^t \boldsymbol{\sigma}_h \mathrm{d}\Omega, \quad (37)$$

for all $k = 1, n_\text{edge}$, $i = 1, n_\text{elem}$ and $a = 1, n_\text{node}$. Equations (35–37) must be supplemented with the velocity and displacement essential boundary conditions. The matrix $\boldsymbol{B}_a$ is the linearized strain operator

$$\boldsymbol{B}_a = \begin{bmatrix} \partial_x \eta_a & 0 \\ 0 & \partial_y \eta_a \\ \partial_y \eta_a & \partial_x \eta_a \end{bmatrix} \quad (38)$$

and the strain and stress tensors are expressed in compact engineering notation:

$$\boldsymbol{\varepsilon} = \begin{bmatrix} \varepsilon_{xx} \\ \varepsilon_{yy} \\ \varepsilon_{xy} + \varepsilon_{yx} \end{bmatrix}, \quad \boldsymbol{\sigma} = \begin{bmatrix} \sigma_{xx} \\ \sigma_{yy} \\ \sigma_{xy}, \end{bmatrix}, \quad (39)$$

for, e.g., the 2D case ($d = 2$). With this notation, the elasticity matrix takes the following form for plane strain:

$$\boldsymbol{D} = \frac{E(1-v)}{(1+v)(1-2v)} \begin{bmatrix} 1 & \frac{v}{1-v} & 0 \\ \frac{v}{1-v} & 1 & 0 \\ 0 & 0 & \frac{1-2v}{2(1-v)} \end{bmatrix}, \quad (40)$$

where E is the Young modulus and v is the Poisson ratio.

3.2 Time discretization

Equations (35–37) are a set of differential–algebraic equations. One can obtain a fully discrete system by further discretizing in time the term:

$$\frac{\partial \zeta_h}{\partial t} \approx \delta_t \zeta_h = \frac{\zeta_h^{n+1} - \zeta_h^n}{\delta t}$$

$$= M^{-1} \frac{p_h^{n+1} - p_h^n}{\delta t} + b \frac{\varepsilon_{V,h}^{n+1} - \varepsilon_{V,h}^n}{\delta t}, \quad (41)$$

and evaluating all other time-dependent terms at some intermediate time $t_{n+\theta}$ with $\theta \in [0,1]$. In practice, we have chosen a fully implicit time discretization (backward Euler, $\theta = 1$).

3.3 Fully discrete coupled system

Introducing the time discretization in the semi-discrete mixed finite element Eqs (35–37), one arrives at the following coupled system of algebraic equations:

$$R_k^v = \int_\Omega \boldsymbol{\psi}_k \cdot \rho_\text{fl} \boldsymbol{g} \mathrm{d}\Omega - \int_{\Gamma_p} \boldsymbol{\psi}_k \cdot \boldsymbol{n} \bar{p} \mathrm{d}\Gamma$$

$$- \int_\Omega \boldsymbol{\psi}_k \cdot (\mathbf{k}/\mu)^{-1} \boldsymbol{v}_h^{n+1} \mathrm{d}\Omega + \int_\Omega \nabla \cdot \boldsymbol{\psi}_k p_h^{n+1} \mathrm{d}\Omega, \quad (42)$$

$$R_i^p = \int_\Omega \varphi_i f \mathrm{d}\Omega - \int_\Omega \varphi_i \nabla \cdot \boldsymbol{v}_h^{n+1} \mathrm{d}\Omega - \int_\Omega \varphi_i \delta_t \zeta_h \mathrm{d}\Omega, \quad (43)$$

$$R_a^u = \int_\Omega \eta_a \rho \boldsymbol{g} \mathrm{d}\Omega + \int_{\Gamma_\sigma} \eta_a \bar{\boldsymbol{t}} \mathrm{d}\Gamma - \int_\Omega \boldsymbol{B}_a^t \boldsymbol{\sigma}_h^{n+1} \mathrm{d}\Omega, \quad (44)$$

to be solved at every time step for the face fluid fluxes $\{V_l^{n+1}\}$, element pressures $\{P_j^{n+1}\}$ and nodal displacements $\{U_b^{n+1}\}$ such that the residuals above are zero. In vector form, the system of $n_\text{face} + n_\text{elem} + d \times n_\text{node}$ algebraic equations can be expressed as follows:

$$\begin{bmatrix} \boldsymbol{R}^v \\ \boldsymbol{R}^p \\ \boldsymbol{R}^u \end{bmatrix} = \begin{bmatrix} \boldsymbol{0} \\ \boldsymbol{0} \\ \boldsymbol{0} \end{bmatrix}. \quad (45)$$

4 Solution strategies

In this section we review different schemes for the solution of the coupled system (45). They vary in the degree of coupling, ranging from a fully coupled approach to a sequential non-iterative approach. We will pay special attention to the choice of the operator split for the sequential solution methods. Even though our model problem is linear, we shall discuss the solution strategies in the more general nonlinear case.

4.1 Fully coupled approach

In the fully coupled approach, the fluxes, pressures and displacements $[\boldsymbol{V}^{n+1}, \boldsymbol{P}^{n+1}, \boldsymbol{U}^{n+1}]$ are sought for simultaneously, using Newton's method. Given an approximation $[\boldsymbol{V}^{n+1}, \boldsymbol{P}^{n+1}, \boldsymbol{U}^{n+1}]^{(k)}$ to the solution at t_{n+1}, an improved solution is obtained as

$$\begin{bmatrix} V^{n+1} \\ P^{n+1} \\ U^{n+1} \end{bmatrix}^{(k+1)} = \begin{bmatrix} V^{n+1} \\ P^{n+1} \\ U^{n+1} \end{bmatrix}^{(k)} + \begin{bmatrix} \delta V^{n+1} \\ \delta P^{n+1} \\ \delta U^{n+1} \end{bmatrix}^{(k)}, \tag{46}$$

where the correction is the solution to the system of linear equations:

$$\begin{bmatrix} S^{vv} & S^{vp} & 0 \\ S^{pv} & S^{pp} & S^{pu} \\ 0 & S^{up} & S^{uu} \end{bmatrix}^{(k)} \begin{bmatrix} \delta V^{n+1} \\ \delta P^{n+1} \\ \delta U^{n+1} \end{bmatrix}^{(k)} = \begin{bmatrix} R^v \\ R^p \\ R^u \end{bmatrix}^{(k)}. \tag{47}$$

The matrix of the system is (minus) the Jacobian matrix. The individual entries of the blocks of this matrix take the following expressions:

$$S_{kl}^{vv} = \int_{\Omega} \boldsymbol{\psi}_k \cdot (\mathbf{k}/\mu)^{-1} \boldsymbol{\psi}_l \mathrm{d}\Omega, \tag{48}$$

$$S_{kj}^{vp} = -\int_{\Omega} \nabla \cdot \boldsymbol{\psi}_k \varphi_j \mathrm{d}\Omega, \tag{49}$$

$$S_{il}^{pv} = \int_{\Omega} \varphi_i \nabla \cdot \boldsymbol{\psi}_l \mathrm{d}\Omega, \tag{50}$$

$$S_{ij}^{pp} = \frac{1}{\delta t} \int_{\Omega} \varphi_i M^{-1} \varphi_j \mathrm{d}\Omega, \tag{51}$$

$$S_{ib}^{pu} = \frac{1}{\delta t} \int_{\Omega} \varphi_i b (\nabla \eta_b)^t \mathrm{d}\Omega, \tag{52}$$

$$S_{aj}^{up} = -\int_{\Omega} \nabla \eta_a b \varphi_j \mathrm{d}\Omega, \tag{53}$$

$$S_{ab}^{uu} = \int_{\Omega} \boldsymbol{B}_a \boldsymbol{D} \boldsymbol{B}_b \mathrm{d}\Omega. \tag{54}$$

The system can be easily symmetrized by multiplying the second block of equations (pressure unknowns) by −1 and the third block of equations (displacement unknowns) by $1/\delta t$. The fully coupled approach is unconditionally stable. Moreover, since the system of equations is linear, Newton's method converges in one iteration.

The flow problem consists in solving for fluxes and pressures simultaneously. For conceptual clarity, we can eliminate the flux unknowns from the first block of Eq. (47):

$$\delta V^{(k)} = (S^{vv})^{-1} \left(R^v - S^{vp} \delta P^{(k)} \right) \tag{55}$$

to arrive at the equivalent 2×2 block system:

$$\begin{bmatrix} \tilde{S}^{pp} & S^{pu} \\ S^{up} & S^{uu} \end{bmatrix} \begin{bmatrix} \delta P \\ \delta U \end{bmatrix}^{(k)} = \begin{bmatrix} \tilde{R}^p \\ R^u \end{bmatrix}^{(k)}, \tag{56}$$

where

$$\tilde{S}^{pp} = S^{pp} - S^{pv}(S^{vv})^{-1}S^{vp}, \tag{57}$$

$$\tilde{R}^p = R^p - S^{pv}(S^{vv})^{-1}R^v. \tag{58}$$

The numerical discretization leading to Eq. (56) may be interpreted as a finite volume method for flow (to be solved for cell-centered pressures), and a finite element method for mechanics (to be solved for nodal displacements). This form of the problem is not used in practice because the matrix $\tilde{S}^{pp}$ is a full matrix, but it simplifies the exposition of the sequential solution schemes.

4.2 Sequential iterative approach (SIA)

As opposed to the fully coupled approach, the iteratively coupled approach solves the system (45) separately for the mechanics (displacements) and flow (fluxes and pressures). An outer iteration is performed to ensure full convergence of the solution at every time step, see Fig. 3.

4.2.1 Drained split

The most obvious operator split for the system (56) is to freeze the pressures during the mechanics solution, and freeze the displacements during the flow solution. This choice of the operator split is sketched graphically in Fig. 4.

As a result, at every outer iteration, one solves the modified system:

$$\begin{bmatrix} \tilde{S}^{pp} & 0 \\ 0 & S^{uu} \end{bmatrix} \begin{bmatrix} \delta P \\ \delta U \end{bmatrix}^{(k)} = \begin{bmatrix} \tilde{R}^p \\ R^u \end{bmatrix}^{(k)}. \tag{59}$$

The drained split is therefore equivalent to a block Jacobi iterative method on the full system [5]. The flow and mechanics problems are effectively decoupled at each
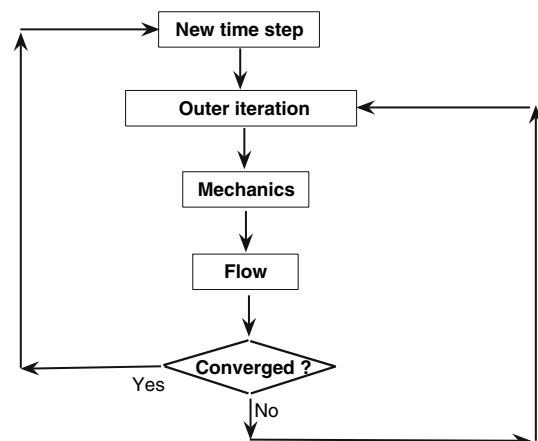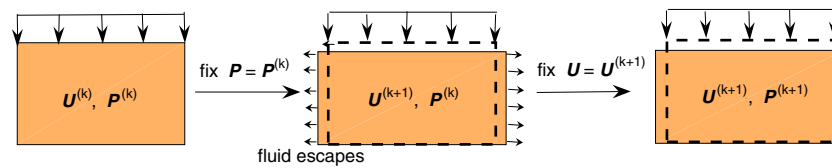

Fig. 3 Flow chart of the sequential iterative approach

Fig. 4 Schematic representation of the drained split

iteration. Alternatively, one could use the updated displacements when solving the flow problem, which amounts to solving

$$\begin{bmatrix} \tilde{S}^{pp} & S^{pu} \\ 0 & S^{uu} \end{bmatrix} \begin{bmatrix} \delta P \\ \delta U \end{bmatrix}^{(k)} = \begin{bmatrix} \tilde{R}^{p} \\ R^{u} \end{bmatrix}^{(k)}, \tag{60}$$

equivalent to a block Gauss–Seidel iteration [5]. Since $\tilde{S}^{pp}$ and S^{uu} are symmetric positive definite matrices, the exact solution is a fixed point and, therefore, if the drained split converges, it converges to the fully coupled solution.

As it turns out, however, this staggered scheme does not preserve the dissipation properties of the coupled system, and renders a solution strategy that is only conditionally stable [3, 4, 42].

4.2.2 Undrained split

An alternative operator split for the system (45) is based on the following physical concept: rather than freezing the pressure during the mechanical step, one can freeze the fluid content. In this way, the mechanical problem is solved while imposing that $\delta m = 0$ for all gridblocks, see Fig. 5. The relevant constitutive equation is then Eq. (11) (with $\zeta = 0$) instead of Eq. (10) (with $\delta p = 0$).

Algebraically, the undrained condition means that $\delta V = 0$ during the mechanical step. Instead of setting $\delta P = 0$, the pressure must vary (locally from element to element), such that

$$\delta P = -\delta P^{*}, \tag{61}$$

where δP^{*} ensures the undrained condition on the second block of Eq. (47):

$$\underbrace{S^{pv}\delta V}_{=0} + S^{pp}\delta P^{*} + S^{pu}\delta U = 0. \tag{62}$$

Substituting this condition into the second block of Eq. (56), we obtain the system of equations for the mechanical step of the undrained split:

$$\left(S^{uu} + S^{up}(S^{pp})^{-1}S^{pu} \right)\delta U = R^{u}. \tag{63}$$

The flow step is performed in the same fashion as in the drained split, using either the previous or updated displacement field, which leads to a modified block Jacobi or a modified block Gauss–Seidel iteration, respectively.

This sequential scheme amounts to solving the system of equations (59) or (60) but with a modified stiffness matrix

$$\tilde{S}^{uu} = S^{uu} + S^{up}(S^{pp})^{-1}S^{pu}. \tag{64}$$

Since this matrix is also symmetric and positive definite, the undrained split (if it converges) converges to the fully coupled solution.

The benefit of this formulation is that it is compatible with the dissipation properties of the physical system and, as a result, it is unconditionally stable [3, 4, 42].

4.3 Sequential non-iterative approach (SNIA)

A non-iterative approach refers to a staggered solution scheme, in which no outer iterations are performed to ensure convergence of the solution at every time step. The solution is advanced by computing one single mechanical solve and one single flow solve per time step. As before, one can use both operator splits described above: the drained and undrained splits.
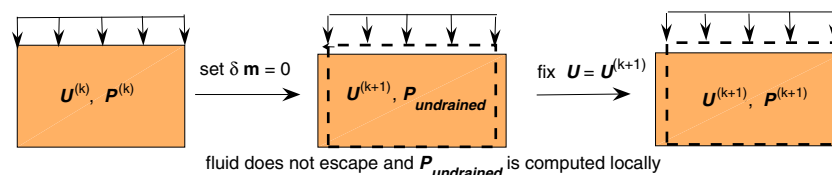
Fig. 5 Schematic representation of the undrained split

5 Representative numerical simulations

The objective of this section is to illustrate the applicability of the formulation to a number of test cases, from validation exercises to more realistic scenarios. The numerical model was implemented in *Diffpack*, a C++ programming environment for simulator development in an object-oriented framework [20].

5.1 Uniaxial compaction test

Our first example is a uniaxial compaction test, simulated under both drained and undrained conditions. The terms drained and undrained conditions refer to whether the fluid is allowed to escape from the sample upon compaction, and are unrelated to the drained and undrained numerical splits (that is, one can simulate an undrained test with a drained sequential scheme, and vice versa).

The model problem is a laterally-constrained specimen, subjected to a uniform compressive traction that is applied suddenly at the top surface. This is the classical Terzaghi problem of consolidation of a finite layer [36]. Since the vertical stress is independent of time, the pore pressure is uncoupled from the stress and satisfies a homogeneous diffusion equation [41]. The solution to the undrained case is very simple: the applied compressive traction will induce an instantaneous pressure build-up and an instantaneous displacement field. These instantaneous changes provide the initial conditions for the drained case, in which pressure and displacement will vary during the pore pressure diffusion phase [41].

Our simulation model is defined in terms of dimensionless quantities, and a sketch of the model is shown in

Table 1 Material parameters for the uniaxial compaction test

Parameter	Symbol	Value
Young modulus	E	100
Poisson ratio	v	0.35
Fluid viscosity	μ	10
Biot coefficient	b	0.9
Biot modulus	M	100
Fluid density	ρ_{fl}	0.8
Total bulk density	ρ	2.2
Permeability	k	1
Porosity	ϕ	0.25

Fig. 6. The dimension of the domain is 0.5×1, discretized with a grid of 100 triangular elements. The lateral displacement is zero along the side boundaries, and so is the vertical displacement at the bottom boundary. A normal compressive traction equal to one is imposed at the top boundary. In the undrained test all boundaries are impervious, whereas in the drained test the top boundary is set at a pressure of –5. This open boundary is modeled by a set of constant-pressure wells at the top row of elements. The material parameters are given in Table 1.
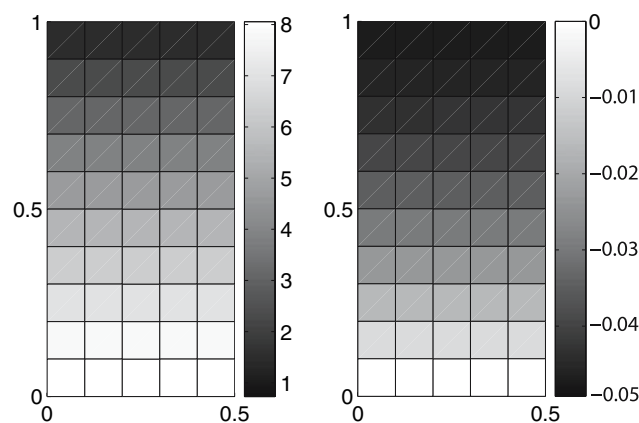
The pressure and displacement fields at steady-state are shown in Figs. 7, 8 for the drained and undrained tests, respectively. The solution agrees with the expected behavior of the system (in fact, with the analytical solution to the problem). In both cases, the maximum deflection occurs at the top boundary, and the pressure field is hydrostatic. The average pressures are of course different in response to the different boundary conditions. The pressure boundary condition in the drained test is such that fluid escapes from the sample, therefore making the system more compressible overall. This explains the larger vertical displacements of the drained test. In Fig. 9 we compare the
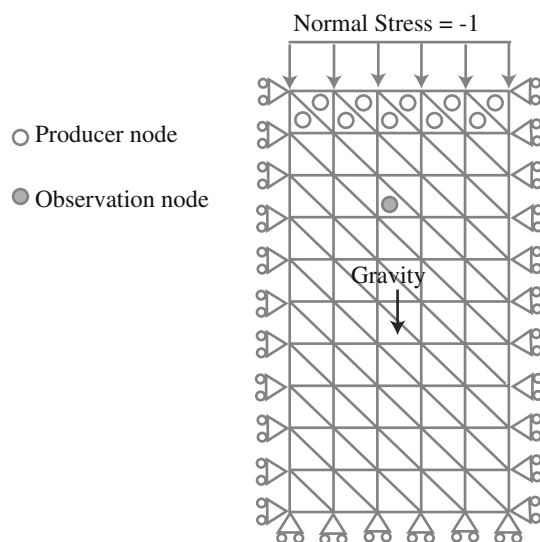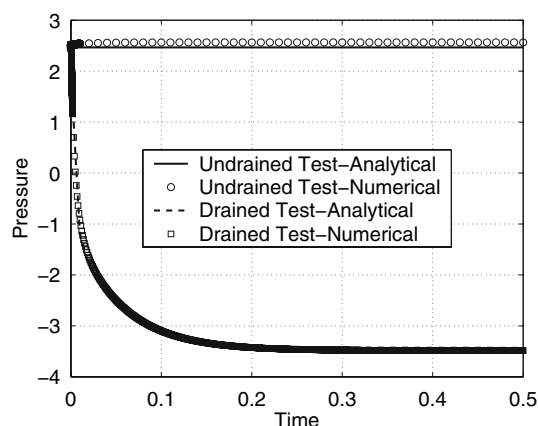
Fig. 6 Definition of the uniaxial compaction test
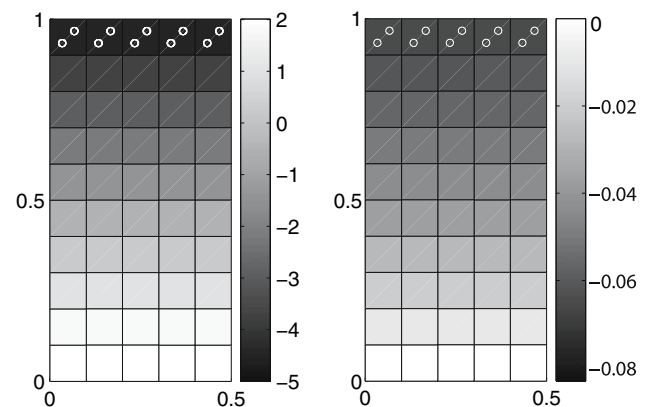
Fig. 7 Pressure (*left*) and displacement (*right*) solution at steady-state for the drained uniaxial compaction test

Fig. 8 Pressure (*left*) and displacement (*right*) solution at steady-state for the undrained uniaxial compaction test
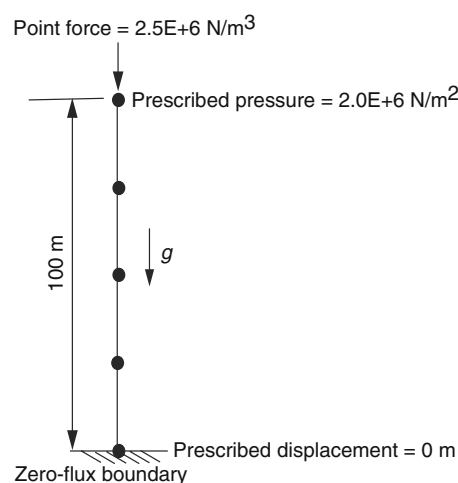

Fig. 9 Evolution of pressure at the observation point for drained and undrained uniaxial compaction tests. Comparison between numerical and analytical solutions

Fig. 10 Sketch of the problem setup for the 1D consolidation problem

Table 2 Material parameters for the 1D consolidation problem

Parameter	Symbol	Value
Overburden stress		2.5 MPa
Top boundary pressure		2.0 MPa
Young modulus	E	1.5 GPa
Poisson ratio	v	0.30
Fluid viscosity	μ	1.0 cP
Biot coefficient	b	0.7
Biot modulus	M	2.5 GPa
Fluid density	ρ_{fl}	1,000 kg/m^3
Total bulk density	ρ	2,400 kg/m^3
Permeability	k	10–1,000 md

evolution of the pressure at the observation point. As expected, the undrained test reaches steady-state almost instantaneously, while the drained test reflects the pressure transient characteristic of fluid withdrawal. In both cases, the agreement with the analytical solution of the problem [41] is excellent.

5.2 Consolidation problem in 1D

Our second example is designed to complement the uniaxial compaction test simulation. The objective is to evaluate the convergence properties of the drained and undrained splits on a simple test case. We use a 1D grid consisting of just four elements, to simulate a consolidation problem. A sketch of the problem is shown in Fig. 10. We impose zero displacement and flux at the bottom boundary. At the top boundary, a prescribed pressure and total stress are imposed. The column is assumed to be in hydrostatic

equilibrium initially. The relevant material properties are listed in Table 2.

Since the top-boundary pressure is prescribed, the fluid is allowed to escape from the system upon application of the point force at the top, and the setup is that of a drained consolidation problem. The question is whether the convergence of the undrained split degrades as the permeability of the medium increases—which makes the poromechanical conditions locally drained.

In Table 3 we report the number of iterations for convergence at time $t = 10^4$ s, using a drained split and an undrained split solution strategy. The convergence criterion is that the L^2-norm of the difference between the solution vectors at successive iterations be less than 10^{-6}. As expected, the number of iterations of the drained split decreases with increasing permeability. We also confirm that the same behavior applies to the undrained split which, moreover, displays accelerated convergence with respect to the drained split—it converges in approximately half the

Table 3 Number of iterations of the drained and undrained splits for the 1D consolidation problem

Permeability (md)	Drained split	Undrained split
10	88	19
50	68	23
100	53	24
200	39	24
1,000	22	25
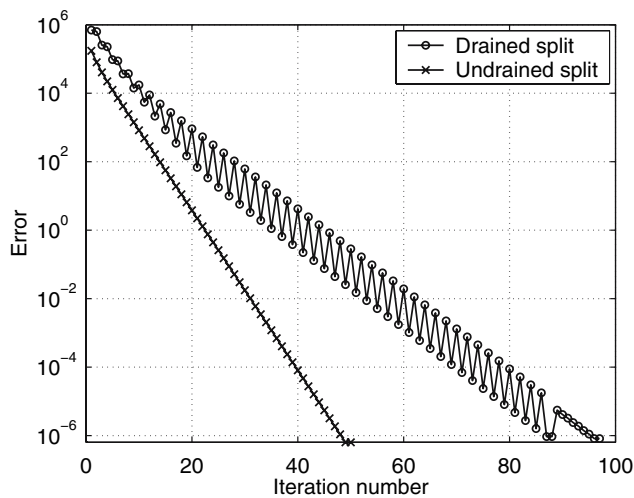
Fig. 11 Evolution of the error for the drained split and the undrained split iterative schemes in the 1D consolidation problem
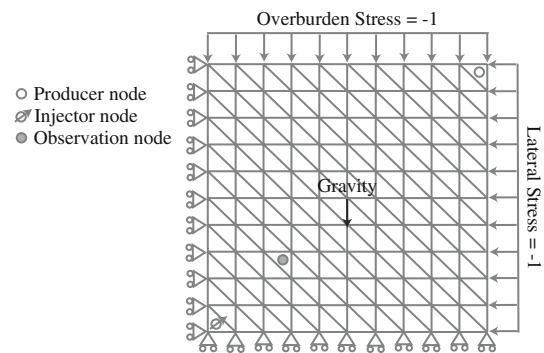

Fig. 12 Sketch of the model problem for the well to well flow example

Table 4 Material parameters for the well to well flow example

Parameter	Symbol	Value
Young modulus	E	100
Poisson ratio	v	0.35
Fluid viscosity	μ	1.0
Biot coefficient	b	0.9
Biot modulus	M	10
Fluid density	ρ_{fl}	1.0
Total bulk density	ρ	2.2
Permeability	k	1
Porosity	ϕ	0.25

number of iterations. In Fig. 11 we plot the evolution of the error for both iterative schemes, for a permeability of 10 md (1 md = 10^{-15} m²). The undrained split converges monotonically, and twice as fast as the drained split.

5.3 Well to well flow pattern

In this example we simulate flow from an injection to a production well, and illustrate the performance of the different solution strategies discussed, with particular emphasis on the behavior of the drained and undrained splits for sequential non-iterative solutions.

The model problem and the boundary conditions are shown in Fig. 12. The domain is a unit square, discretized into 200 triangular elements. All boundaries are impervious, and prescribed-pressure injection ($p_{\text{inj}} = 10$) and production ($p_{\text{prod}} = -10$) wells are placed at the bottom–left and top–right elements, respectively. The material parameters are given in Table 4.

In Figs. 13, 14 we show the pressure field and the velocity field, respectively, for runs with and without gravity. In this case, the pressure field is dominated by the well-to-well flow, and the influence of gravity is relatively
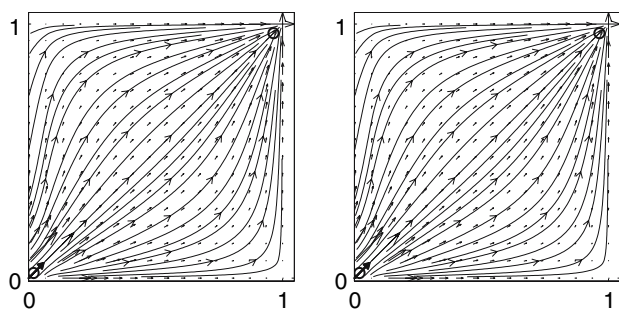
minor. The results in these two figures have been computed with the fully coupled approach.

To analyze the effect of different coupling strategies we compare the results from the sequential non-iterative approach using drained and undrained splits with the fully coupled solution. The evolution of pressure and vertical displacement at the observation node computed with the different solution schemes is shown in Figs. 15, 16, respectively. We make the following observations:

1. *Stability of the drained and undrained splits.* It is clear that with a time step of $\delta t = 0.1$, the non-iterative undrained split solution is stable and virtually identical to the fully coupled solution. In this particular case, the computational cost of the sequential solution was about five times less than the fully coupled solution. In contrast, and for the same time step, the drained split results in wild oscillations during the initial transient, both in pressure and displacement. Refining the time step removes the oscillatory behavior (at the cost, of course, of much longer simulation time). Although oscillations could also arise from the use of a low-dissipation time stepping technique such as the Crank-Nicolson method, the oscillatory behavior observed
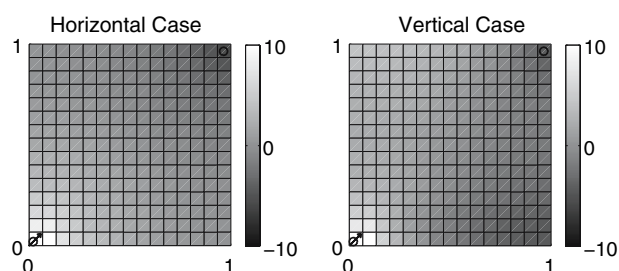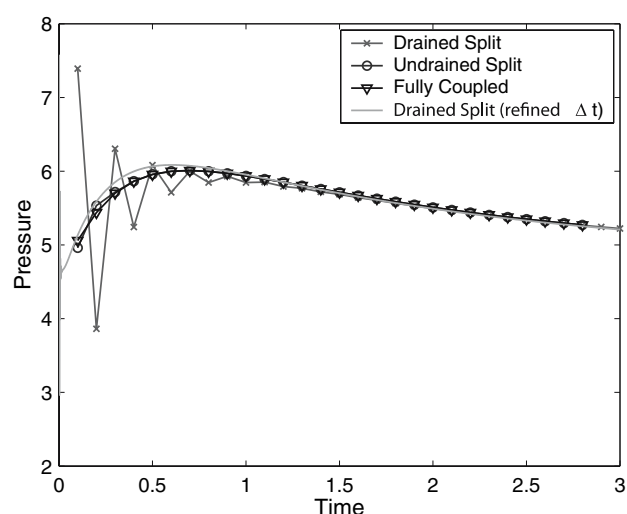
Fig. 13 Pressure field for horizontal and vertical cases

Fig. 14 Streamlines for horizontal and vertical cases

Fig. 15 Comparison of evolution of pressure at observation point for drained and undrained splits

Fig. 16 Comparison of evolution of vertical displacement at observation point for drained and undrained splits

here is related to the conditional stability of the drained split—indeed, the fully coupled solution does not show oscillations. The reason why the drained split does not yield divergent results is that, in this example, the most challenging time step (that tests stability) is the first time step, because flow is driven by a sudden change in well pressure at $t = 0$. In fact, we observe that if the time step δt is larger than some critical value, the drained split does not converge for the first time step. Imposing the well flow rate instead of the well pressure would result in a system that is disturbed continuously, and divergence would occur later in the simulation.
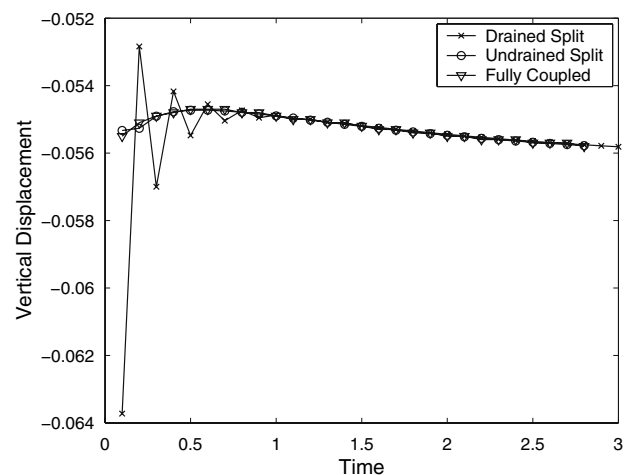
2. *Mandel–Cryer effect*. An interesting feature of the system is the presence of a hump in the time evolution of the pressure. This non-monotonic behavior of the pressure, known as the Mandel–Cryer effect, is characteristic of the coupled poromechanics problem, and cannot be reproduced in flow simulations that ignore the two-way coupling with the mechanical response of the porous medium.

5.4 Application to a synthetic reservoir

We now present a slightly more realistic case, modeling a cross section of a synthetic reservoir. The model problem is shown in Fig. 17. The problem dimensions and material parameters now have units and realistic values. The size of the domain is $3{,}000 \times 800$ m. The logarithm of the permeability field is shown in Fig. 18. It has a layered struc-

ture and varies over three orders of magnitude. Wells have multi-block completions with the injector having a fixed bottom hole pressure control and the producer having a fixed rate control. The injector is open to 10 gridblocks near the bottom of the reservoir, whereas the producer is open to 5 blocks roughly in the middle of the reservoir. The material properties and other parameters of the simulation are compiled in Table 5.

The pressure and velocity fields after 20 days of simulation time are shown in Figs. 19, 20, respectively. From these plots it is apparent that most of the fluid flows through a rather narrow high-permeability region connecting injector and producer.

In Fig. 21 we plot the stress ratio (the ratio of the equivalent von Mises effective stress to mean normal effective stress) on the deformed grid (exaggerated for
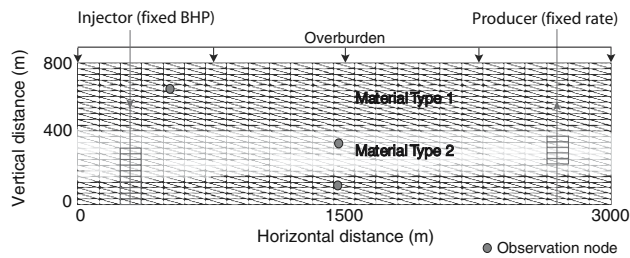
Fig. 17 Problem setting for the synthetic reservoir model
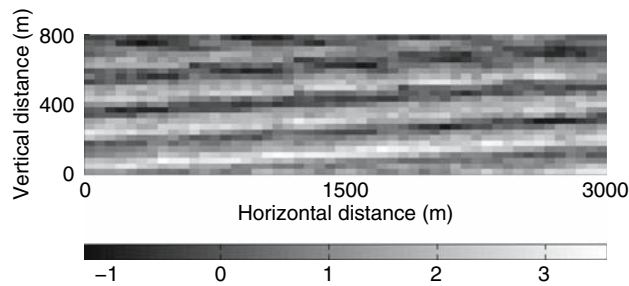
**Fig. 18** Log-permeability map for the synthetic reservoir model, in md

Table 5 Material parameters for the synthetic reservoir model

| Parameter	Symbol	Value
Initial stress	σ_0	10 MPa
Overburden stress		10 MPa
Young modulus	E	10 MPa
Poisson ratio	v	0.35
Fluid viscosity	μ	1.0 cP
Biot coefficient	b	0.9
Biot modulus	M	10 MPa
Fluid density	ρ_{fl}	800 kg/m^3
Total bulk density	ρ	2,200 kg/m^3
Permeability	k	1–1,000 md
Porosity	ϕ	0.25
Injector BHP		50 MPa
Producer rate		100 m^3/day

visual contrast). In this case, the zone with the highest equivalent stress is the area around the injector. In real scenarios, this type of analysis could give a zeroth-order indicator of potential problems of wellbore collapse, sand production, or fracturing of geologic layers.
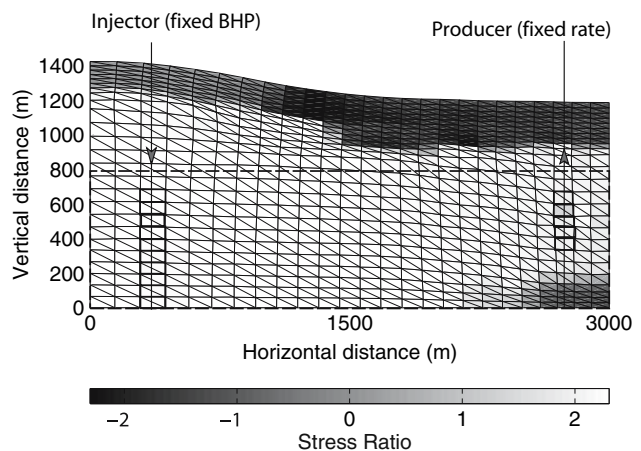
6 Conclusions

We have presented a new approach for the simulation of coupled reservoir geomechanics. The technical aspects that make our approach unique are:
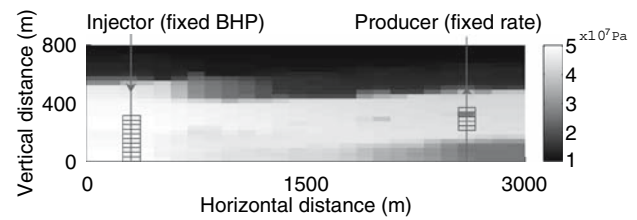
Fig. 19 Pressure field for the synthetic reservoir model
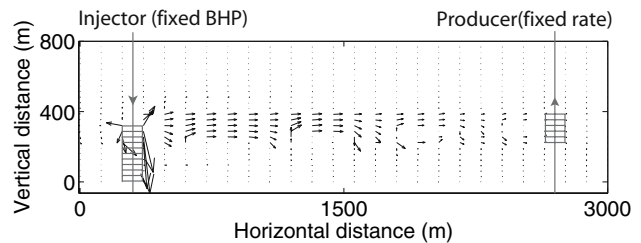
Fig. 20 Velocity field for the synthetic reservoir model

Fig. 21 Stress ratio for the synthetic reservoir model on an exaggerated deformed grid

1. *The space discretization of the equations*. The unknown variables are the pressure, the fluid velocity, and the rock displacements. We recognize that these variables are of very different nature, and need to be discretized *differently*. We propose a mixed finite element space discretization, which is stable, convergent, locally mass conservative, and employs a single computational grid. To ensure stability and robustness, we perform an implicit time integration of fluid flow equations.

2. *The strategies for the solution of the coupled system*. We compare different solution strategies, including the fully coupled approach, the usual (conditionally stable) iteratively coupled approach based on a drained split, and a less standard sequential scheme based on an

undrained split, which is unconditionally stable. The examples in this paper illustrate the benefit of the undrained-split sequential solution scheme.

3. *The implementation in a reservoir simulator.* The numerical model was implemented in an object oriented fashion using the *Diffpack* computational environment, making it amenable to extensions.

The scope of this paper was limited to single-phase linear poroelasticity. Clearly, this is insufficient for the simulation and prediction of many reservoir and near-well geomechanical processes, which will require the following extensions: (1) 3D problems; (2) inelastic deformations, through efficient return-mapping algorithms [33]; (3) multiphase flow, to be discretized using a finite volume scheme and through a sequential solution method; (4) coupling with micromechanical approaches for modeling post-failure (often softening) behavior.

References

1. Aadnoy BS, Ong S (2003) Introduction to the special issue on Borehole Stability. J Pet Sci Eng 38:79–82
2. Allen DR (1968) Physical changes of reservoir properties caused by subsidence and repressurizing operations, Wilmington field, California. J Pet Technol 20(1):23–29
3. Armero F (1999) Formulation and finite element implementation of a multiplicative model of coupled poro-plasticity at finite strains under fully saturated conditions. Comput Methods Appl Mech Eng 171:205–241
4. Armero F, Simo JC (1992) A new unconditionally stable fractional step method for coupled thermomechanical problems. Int J Numer Methods Eng 35:737–766
5. Axelsson O (1994) Iterative solution methods. Cambridge University Press, Cambridge
6. Babuška I (1973) The finite element method with Lagrangian multipliers. Numer Math 20:179–192
7. Biot MA (1941) General theory of three-dimensional consolidation. J Appl Phys 12:155–164
8. Brenner SC, Scott LR (1994) The mathematical theory of finite element methods, volume 15 of Texts in Applied Mathematics. Springer, Heidelberg
9. Brezzi F (1974) On the existence, uniqueness and approximation of saddle point problems arising from Lagrange multipliers. RAIRO Anal Numér 8:129–151
10. Brezzi F, Fortin M (1991) Mixed and hybrid finite element methods, volume 15 of Springer Series in Computational Mathematics. Springer, Heidelberg
11. Chin LY, Raghavan R, Thomas LK (2000) Fully coupled analysis of well responses in stress-sensitive reservoirs. SPE Reserv Eval Eng 3(5):435–443
12. Coussy O (1991) Mechanics of Porous Media. Wiley, Chichester, 1995. Originally published in French as Mécanique des Milieux Poreux, Editions Technip
13. Dean RH, Gai X, Stone CM, Minkoff SE (2006) A comparison of techniques for coupling porous flow and geomechanics. Soc Pet Eng J 11(1):132–140
14. Fredrich JT, Arguello JG, Deitrick GL, de Rouffignac EP (2000) Geomechanical modeling of reservoir compaction, surface subsidence, and casing damage at the Belridge diatomite field. SPE Reserv Eval Eng 3(4):348–359
15. Gutierrez M, Lewis RW, Masters I (2001) Petroleum reservoir simulation coupling fluid flow and geomechanics. SPE Reserv Eval Eng 4(3):164–172
16. Han G, Stone T, Liu Q, Cook J, Papanastasiou P (2005) 3-D elastoplastic FEM modelling in a reservoir simulator. In: SPE Reservoir Simulation Symposium, Houston, 31 January–2 February 2005. (SPE 91891)
17. Hermansen H, Thomas LK, Sylte JE, Aasboe BT (1997) Twenty five years of Ekofisk reservoir management. In: SPE Annual Technical Conference and Exhibition, San Antonio, 5–8 October 1997. (SPE 38927)
18. Huang M, Zienkiewicz OC (1998) New unconditionally stable staggered solution procedures for coupled soil-pore fluid dynamic problems. Int J Numer Methods Eng 43:1029–1052
19. Jha B (2005) A mixed finite element framework for modeling coupled fluid flow and reservoir geomechanics. MS Thesis, Petroleum Engineering, Stanford University
20. Langtangen HP (2003) Computational partial differential equations: numerical methods and Diffpack programming, 2nd edn. Springer, Heidelberg
21. Lewis RW, Schrefler BA (1998) The finite element method in the static and dynamic deformation and consolidation of porous media, 2nd edn. Wiley, Chichester
22. Lewis RW, Sukirman Y (1993) Finite-element modeling of 3-phase flow in deforming saturated oil-reservoirs. Int J Numer Anal Methods Geomech 17(8):577–598
23. Li X, Mitchum FL, Bruno M, Patillo PD, Willson SM (2003) Compaction, subsidence, and associated casing damage and well failure assessment for the Gulf of Mexico shelf Matagorda Island 623 field. In: SPE Annual Technical Conference and Exhibition, Denver, 5–8 October 2003. (SPE 84553)
24. Li X, Zienkiewicz OC (1992) Multiphase flow in deforming porous media and finite element solutions. Comput Struct 45(2):211–227
25. Liu Q, Stone T, Han G, Marsden R, Shaw G (2004) Coupled stress and fluid flow using a finite element method in a commercial reservoir simulator. In: SPE Asia Pacific Oil and Gas Conference and Exhibition, Perth, 18–20 October 2004. (SPE 88616)
26. Minkoff SE, Stone CM, Bryant S, Peszynska M, Wheeler MF (2003) Coupled fluid flow and geomechanical deformation modeling. J Pet Sci Eng 38:37–56
27. Osorio JG, Chen H-Y, Teufel LW, Shaffer S (1998) A two-domain, 3D, fully coupled fluid-flow/geomechanical simulation model for reservoirs with stress-sensitive mechanical and fluid-flow properties. In: SPE/ISRM Eurock '98, Trondheim, 8–10 July 1998. (SPE/ISRM 47397)
28. Park KC (1983) Stabilization of partitioned solution procedure for pore fluid–soil interaction analysis. Int J Numer Methods Eng 19(11):1669–1673
29. Raviart PA, Thomas JM (1977) A mixed finite element method for second order elliptic problems. In: Galligani I, Magenes E (eds) Mathematical aspects of the finite element method, volume 606 of Lecture Notes in Mathematics. Springer, Heidelberg, pp 292–315
30. Settari A, Mourits FM (1998) A coupled reservoir and geomechanical simulation system. Soc Pet Eng J 3(3):219–226
31. Settari A, Walters DA (2001) Advances in coupled geomechanical and reservoir modeling with applications to reservoir compaction. Soc Pet Eng J 6(3):334–342

32. Shaw G, Stone T (2005) Finite volume methods for coupled stress/fluid flow in a commercial reservoir simulator. In: SPE reservoir simulation symposium, Houston, 31 January–2 February 2005. (SPE 93430)

33. Simo JC, Hughes TJR (1998) Computational inelasticity, volume 7 of Interdisciplinary Applied Mathematics. Springer, Heidelberg

34. Stone T, Bowen G, Papanastasiou P, Fuller J (2000) Fully coupled geomechanics in a commercial reservoir simulator. In: SPE European petroleum conference, Paris, 24–25 October 2000. (SPE 65107)

35. Stone TW, Xian C, Fang Z, Manalac E, Marsden R, Fuller J (2003) Coupled geomechanical simulation of stress dependent reservoirs. In: SPE Reservoir Simulation Symposium, Houston, 3–5 February 2003. (SPE 79697)

36. Terzaghi K (1943) Theoretical soil mechanics. Wiley, New York

37. Thomas LK, Chin LY, Pierson RG, Sylte JE (2003) Coupled geomechanics and reservoir simulation. Soc Pet Eng J 8(4):350–358

38. Tran D, Settari A, Nghiem L (2002) New iterative coupling between a reservoir simulator and a geomechanics module. In: SPE/ ISRM rock mechanics conference, Irving, 20–23 October 2002. (SPE 78192)

39. Wan J (2002) Stabilized finite element methods for coupled geomechanics and multiphase flow. PhD Dissertation, Petroleum Engineering, Stanford University

40. Wan J, Durlofsky LJ, Hughes TJR, Aziz K (2003) Stabilized finite element methods for coupled geomechanics–reservoir flow simulations. In: SPE reservoir simulation symposium, Houston, 3–5 February 2003. (SPE 79694)

41. Wang HF (2000) Theory of linear poroelasticity. Princeton University Press, Princeton, New Jersey

42. Zienkiewicz OC, Paul DK, Chan AHC (1988) Unconditionally stable staggered solution procedure for soil–pore fluid interaction problems. Int J Numer Methods Eng 26(5):1039–1055

43. Zoback MD, Barton CA, Brudy M, Castillo DA, Finkbeiner T, Grollimund BR, Moos DB, Peska P, Ward CD, Wiprut DJ (2003) Determination of stress orientation and magnitude in deep wells. Int J Rock Mech Min Sci 40:1049–1076